Research Square

Preprints are preliminary reports that have not undergone peer review.
They should not be considered conclusive, used to inform clinical practice,
or referenced by the media as validated information.

A Self-Powered Ultrafast Polarization-Sensitive Multifunctional Photodetector Driven by Phonon Anisotropy in a PtSe2/MoSe2 Heterostructure

Mukesh kumar

mkumar@iitrpr.ac.in

Indian Institute of Technology Ropar https://orcid.org/0000-0001-6389-2040

Priya Rani

Indian Institute of Technology Ropar

Rohit Dahiya

Indian Institute of Technology Ropar

Chaitanya Auti

Indian Institute of Technology Mandi

Pradeep Kumar

Indian Institute of Technology Mandi, H.P., India

Article

Keywords:

Posted Date: April 6th, 2026

DOI: https://doi.org/10.21203/rs.3.rs-9038386/v1

License: This work is licensed under a Creative Commons Attribution 4.0 International License.
Read Full License

Additional Declarations: There is **NO** Competing Interest.

A Self-Powered Ultrafast Polarization-Sensitive Multifunctional Photodetector Driven by Phonon Anisotropy in a $PtSe_2/MoSe_2$ Heterostructure

Priya Rani[1,2], Rohit Dahiya[1], Chaitanya B. Auti[2], Pradeep Kumar[2*] and Mukesh Kumar[1*]

[1]Functional and Renewable Energy Materials Laboratory, Department of Physics, Indian Institute of Technology Ropar, Rupnagar, Punjab – 140001, India

[2]School of Physical Sciences, Indian Institute of Technology Mandi, Mandi-175005, India.

*Corresponding email – mkumar@iitrpr.ac.in , pkumar@iitmandi.ac.in

Abstract

Polarization-sensitive photodetectors (PSPDs) have attracted significant interest due to their ability to detect both the polarization state and intensity of light, thereby increasing information dimensionality for compact remote sensing, imaging, and communication systems. Conventional polarization-sensitive detectors rely on external polarization optical components, resulting in bulky device structures, complex architectures, and high cost. Herein, we report a self-powered, PSPD based on a $PtSe_2/MoSe_2$ van der Waals heterostructure. The semimetal/semiconductor integration enables broadband photoresponse spanning 400-1200 nm with excellent polarization sensitivity. Angle-resolved polarized Raman spectroscopy confirms that interlayer coupling arising from heterostructure formation enhances phonon vibrational anisotropy, leading to stronger optical anisotropy compared to bare $PtSe_2$. A remarkable polarization ratio of ~38 is obtained under self-bias operation. Efficient interlayer charge transport results in ultrafast response times of 66 μs at zero bias and 6 μs under a 5 V bias. Furthermore, the photodetector delivers a self-biased responsivity of 0.74 mA W^{-1} and a detectivity of 10^{10} Jones. Notably, bias-tunable polarization sensitivity and wavelength-dependent anisotropy further enhance imaging and target-detection capabilities. These results

highlight the promise of two-dimensional transition metal dichalcogenides (TMDC) heterostructures for next-generation multidimensional imaging and integrated optoelectronic technologies.

Introduction

Multifunctional photodetectors (PDs) are essential components of modern optoelectronic systems, enabling the simultaneous detection of multiple optical parameters[1, 2, 3, 4, 5]. Among these, self-driven polarization-sensitive photodetectors (self-PSPDs) have recently garnered considerable attention because they can detect both the intensity and polarization state of incident light without requiring an external bias[6, 7, 8]. In such devices, polarization information is directly resolved at the detector through intrinsic mechanisms such as anisotropic crystal structure, engineered electrode configurations, or built-in junction electric fields[9, 10]. As a result, external polarization optics, such as polarizers or analyzers, are no longer necessary, enabling more compact, energy-efficient, and integrated photodetection systems. This dual functionality enables low-power systems for diverse applications, including remote sensing, polarization imaging, environmental monitoring, and defence technologies[11, 12, 13]. Conventional polarization-sensitive photodetectors based on III-V compound semiconductors or other narrow-bandgap materials, such as indium antimony (InSb), mercury cadmium telluride (HgCdTe), and indium gallium arsenide (InGaAs), have demonstrated excellent performance across different wavelength bands[14, 15, 16]. However, these technologies have several significant disadvantages, including complex manufacturing processes, a requirement for cryogenic temperatures, and a reliance on bulky polarization optics that hinder miniaturization and scalability[8, 17, 18].

Two-dimensional (2D) materials with tunable band gaps, strong light-matter interactions, high carrier mobility, structural anisotropy, and seamless compatibility with silicon-based

technologies make them a promising candidate for next-generation polarization-sensitive photodetectors[8, 19, 20, 21, 22]. Low-symmetry 2D materials such as black phosphorus (BP), black arsenic phosphorus (b-AsP), GeSe, $PdSe_2$, $ReSe_2$, etc., enable polarizer-free polarization detection owing to their intrinsic in-plane anisotropy, offering a compact route toward polarization-sensitive photodetectors[23, 24, 25, 26]. Despite this advantage, their performance is often limited by poor air stability, external bias requirements, a narrow detection bandwidth, and a relatively low polarization ratio, which significantly hampers their further development and real-world applications[20, 27, 28, 29]. In this context, Platinum diselenide ($PtSe_2$), a group-10 TMDC with intrinsic anisotropy, high ambient air stability, high carrier mobility, and a widely tunable bandgap (1.2 eV in monolayer and semi-metallic in multilayer/bulk), is the best-suited candidate for the synthesis of a highly sensitive polarization photodetector[30, 31]. However, the semi-metallic character of multilayer $PtSe_2$ leads to high dark current and a limited on–off ratio, which remain major bottlenecks for device performance[32]. To address the above shortcomings, fabricating its van der Waals (vdW) heterostructure with a suitable candidate is the best possible approach[3, 27, 33]. Thus, by using a heterojunction, we can leverage the advantages of both materials, leading to increased device performance compared to either material alone[34]. For example, Dong *et al.* [32] fabricated a BP/$PtSe_2$ van der Waals heterostructure and demonstrated a polarization-sensitive Mid-IR photodetection. The fabricated heterostructure shows self-powered operation with a response speed of 370/300 μs and a specific detectivity of ~ 2.5×10^9 cm $Hz^{0.5}$ W^{-1}; however, the polarization ratio was limited to only ~ 0.9. Similarly, Kang *et al.*[35] demonstrated the $PdSe_2$/$PtSe_2$ heterostructure with a peak responsivity of 1.232 A W^{-1} (at 532 nm under a bias of -2 V), specific detectivity of 9.82×10^9 Jones (at 1310 nm), rise/fall times of 6.13/32.88 μs, and a polarization ratio of only ~1.07 at 532 nm. Notably, most heterostructure devices rely on mechanical exfoliation followed by wet or dry transfer, which inevitably introduces interfacial contamination and defects, limits wafer-scale scalability, and

compromises device reproducibility[30, 31]. Therefore, the development of scalable, high-quality multifunctional photodetectors with enhanced polarization sensitivity, low dark current, and self-powered operation remains a critical challenge.

In this context, we demonstrate a transfer-free, large-area $PtSe_2/MoSe_2$ vdW heterostructure-based photodetector fabricated via the thermally assisted conversion (TAC) method. $MoSe_2$ is primarily chosen because it exhibits a thickness-dependent bandgap tunable from ~1.6 eV in the monolayer to ~1.1 eV in the bulk, along with strong light absorption, long carrier lifetimes, and high photodetection sensitivity[7, 36, 37, 38, 39]. The fabricated heterostructure device exhibits efficient polarization sensitivity with a very high polarization ratio (PR) of ~38 at a 650 nm laser, representing a significant improvement over previously reported polarization-sensitive 2D/2D heterostructures [7, 11, 40, 41, 42, 43]. Angle-resolved polarized Raman spectroscopy (ARPRS) confirms the enhanced phonon vibrational anisotropy induced by heterostructure formation relative to bare $PtSe_2$. Notably, the device exhibits bias-tunable polarization sensitivity and wavelength-dependent anisotropy. Importantly, the rotation of polarization-resolved photocurrent maxima with incident photon energy evidences intrinsic wavelength-dependent anisotropy and highlights the tunable anisotropic photoresponse of the $PtSe_2/MoSe_2$ heterostructure. Furthermore, room-temperature polarization-resolved imaging underscores its multifunctional capability. Along with the polarization sensitivity, the heterostructure demonstrates a broadband (400 nm – 1200 nm) self-powered operation with a peak responsivity of 0.74 mA W^{-1} and a specific detectivity in the order of 10^{10} Jones at 800 nm. Also, the heterostructure device achieves a 27-fold increase in responsivity over bare $MoSe_2$, reaching 0.23 A/W at 800 nm (5 V bias). Remarkably, this device achieves ultrafast response of 68/66 μs (rise/fall time) at 650 nm laser under self-bias, which further improves to 6/6 μs under a moderate bias of 5V. The band alignment at the $PtSe_2/MoSe_2$ interface is systematically analysed using X-ray photoelectron spectroscopy, enabling a comprehensive understanding of

charge-transfer dynamics. The working mechanism of the $PtSe_2/MoSe_2$ heterojunction under 0V bias conditions is discussed in detail. These results establish a viable pathway toward scalable, transfer-free, multifunctional 2D/2D vdW heterostructures for high-performance, self-powered, polarization-sensitive photodetectors, with strong potential for next-generation optoelectronic, imaging and communication applications.

Experimental section

Synthesis of $MoSe_2$ film by the TAC method: $MoSe_2$ thin films were synthesised using a TAC method on a SiO_2/Si substrate. The substrates (1.5×1.5 cm^2) were first cleaned sequentially by ultrasonic treatment in soap solution, deionised water (DI), acetone, and isopropanol for 30 minutes each, followed by N_2 blow-drying. Figure S1(a) depicts the synthesis procedure for the $MoSe_2$ thin film. Molybdenum (Mo) film was first deposited on these cleaned substrates via RF magnetron sputtering using a high-purity Mo target (99.95%) at a power of 30 W for 2 minutes, after reaching a base pressure of 7×10^{-7} Torr at room temperature. Next, the Mo-coated substrates ($Mo/SiO_2/Si$) were selenized in a chemical vapor deposition (CVD) system using selenium powder. For that, the Mo-coated substrate and selenium (Se) powder were placed 14 cm apart in a small quartz tube, which was inserted into a bigger tube equipped with a 3-zone furnace. Before selenization, the furnace was purged with 300 sccm of 1.1% H_2 balance Ar gas for 30 minutes to remove residual oxygen and moisture; after that, the gas flow was switched to 75 sccm during deposition. The temperature of zone 1 (Se powder) was maintained at 350˚C at a ramp rate of 10˚C/min for 30 minutes, while zone 2 (Mo-coated substrate) was heated to 500˚C with a ramp rate of 12.5˚C/min for 45 minutes, followed by natural cooling to room temperature. The temperature profile is shown in Figure 1 S(b).

Synthesis of 2D $PtSe_2/MoSe_2$ heterostructure device: For heterostructure formation, an ultra-thin Pt layer was deposited on half of the $MoSe_2$ film (while the other half was physically

shadowed) using RF magnetron sputtering for 0.5 minutes at 30 W, with a deposition pressure of 3.75 mTorr at room temperature. Subsequently, these Pt-coated $MoSe_2$ ($Pt/MoSe_2/SiO_2/Si$) samples were selenized in CVD under the same conditions and parameters used for the $MoSe_2$ film to form the layered $PtSe_2/MoSe_2$ heterostructure. Finally, for the device fabrication, gold (Au) strip electrodes (3.5 mm inter-strip spacing) were deposited via thermal evaporation using a physical shadow mask, as shown in Figure 1(a). The actual image of the $PtSe_2/MoSe_2$ heterostructure device, measuring approximately 1.5×1.5 cm^2, is shown in Figure S1(c), demonstrating the transfer-free growth of a large-area device.

Characterization

Raman spectroscopy and angle-resolved polarized Raman spectroscopy (ARPRS) were performed at room temperature using a 532 nm laser on a HORIBA LabRAM HR Evolution spectrometer in backscattering configuration. ARPRS was performed by placing a half-wave plate near the laser entrance to continuously rotate the polarization of the incident light on the sample, while the analyzer used to select the polarization of the scattered light was kept fixed. This configuration enabled a systematic investigation of phonon vibrational anisotropy. An atomic force microscope (AFM) was performed in tapping mode using a Bruker (Multimode 8) Scanning Probe Microscope to measure the thickness of different layers. The optical images were captured using the Nikon ECLIPSE LV100ND instrument. Optical absorption spectra were measured using a Perkin Elmer Lambda 950 UV–Vis–NIR spectrophotometer. X-ray Photoelectron Spectroscopy (XPS) measurements were performed using a Thermo Fisher Scientific ESCALAB Xi^+ system with Al Kα radiation as the X-ray source.

Photodetector performance was evaluated using a Bentham PVE 300 monochromator, in conjunction with a Keithley 6430 Source Measure Unit (SMU), over the 400–1200 nm spectral range. The temporal photoresponse of the devices was measured under 532 nm and 650 nm laser

illumination using HOLMARC laser sources coupled with an optical chopper, and the response was monitored on an oscilloscope. Polarization-dependent studies employed the lasers with an additional polarizer.

Results and Discussion

A schematic diagram of the $PtSe_2/MoSe_2$ heterostructure photodetector device is shown in Figure 1(b). The optical image in Figure 1(c) shows a distinct boundary between the $MoSe_2$ and $PtSe_2$ thin-film regions, confirming the successful stacking of the two layers. The structural quality of the films was examined by Raman spectroscopy with 532 nm excitation. Figure 1(d) shows the Raman spectra of pristine $MoSe_2$, $PtSe_2$, and $PtSe_2/MoSe_2$ heterostructure. The Raman spectra of $MoSe_2$ exhibit peaks at ~239.8 cm^{-1}, ~167.4 cm^{-1}, and ~286.6 cm^{-1}, corresponding to the A_{1g} (out-of-plane vibration), E_{1g} and E^1_{2g} (in-plane vibration) symmetry, respectively, [31, 39]. In the $PtSe_2$ layer, Raman spectra display its characteristic A_{1g} (~205.4 cm^{-1}), E_g (~176.4 cm^{-1}) vibrational modes and a weak longitudinal optical (LO) mode at ~230 cm^{-1} [44, 45, 46]. In addition, the Raman spectra of $PtSe_2/MoSe_2$ heterojunction exhibit characteristic peaks of $MoSe_2$ and $PtSe_2$, confirming the successful formation of the van der Waals heterostructure. Furthermore, the A_{1g} mode of $PtSe_2$ shows a redshift of about ~1.8 cm^{-1} in the heterostructure, suggesting interlayer strain and the strong coupling at the heterojunction[30]. Angle-resolved polarized Raman spectroscopy (ARPRS) was employed to investigate the phonon vibrational anisotropy of $PtSe_2$ and $PtSe_2/MoSe_2$ heterostructure. The Raman spectra were collected by varying the polarization direction of incident light from 0˚ to 360˚ with a step size of 10˚. Figure S2(a-b) illustrates the polarized Raman spectra of $PtSe_2$, where the A_{1g} (~205 cm^{-1}) and E_g (~176.4 cm^{-1}) vibrational modes exhibit a clear periodic variation in intensity with polarization angle, confirming intrinsic vibrational phonon anisotropy in the film. Figure 1(e) shows the angle-dependent false-colour intensity mapping image of $PtSe_2/MoSe_2$ heterostructure, revealing strong 180˚ periodic modulation in Raman peaks at ~169,

~178, ~207, ~239, and ~285 cm^{-1}. There is a clear variation in peak intensities along with noticeable peak shifts after heterostructure formation, confirming the anisotropic nature of the coupled system[47]. Furthermore, to reveal the relationship between the angle-resolved Raman spectra and the crystal orientation, the peak intensities of the A_{1g} mode were extracted and plotted into corresponding polar graphs, as shown in Figure 1(f). The angular dependence of the Raman intensity was fitted using Raman tensor analysis (supplementary note S1) [48]. This pronounced anisotropy in the heterostructure is attributed to interlayer coupling between $PtSe_2$ and $MoSe_2$ layers, which modifies the symmetry of the system and enhances optical anisotropy. Such coupling plays a key role in the superior polarization sensitivity observed in the $PtSe_2/MoSe_2$ heterostructure device[30, 49, 50].

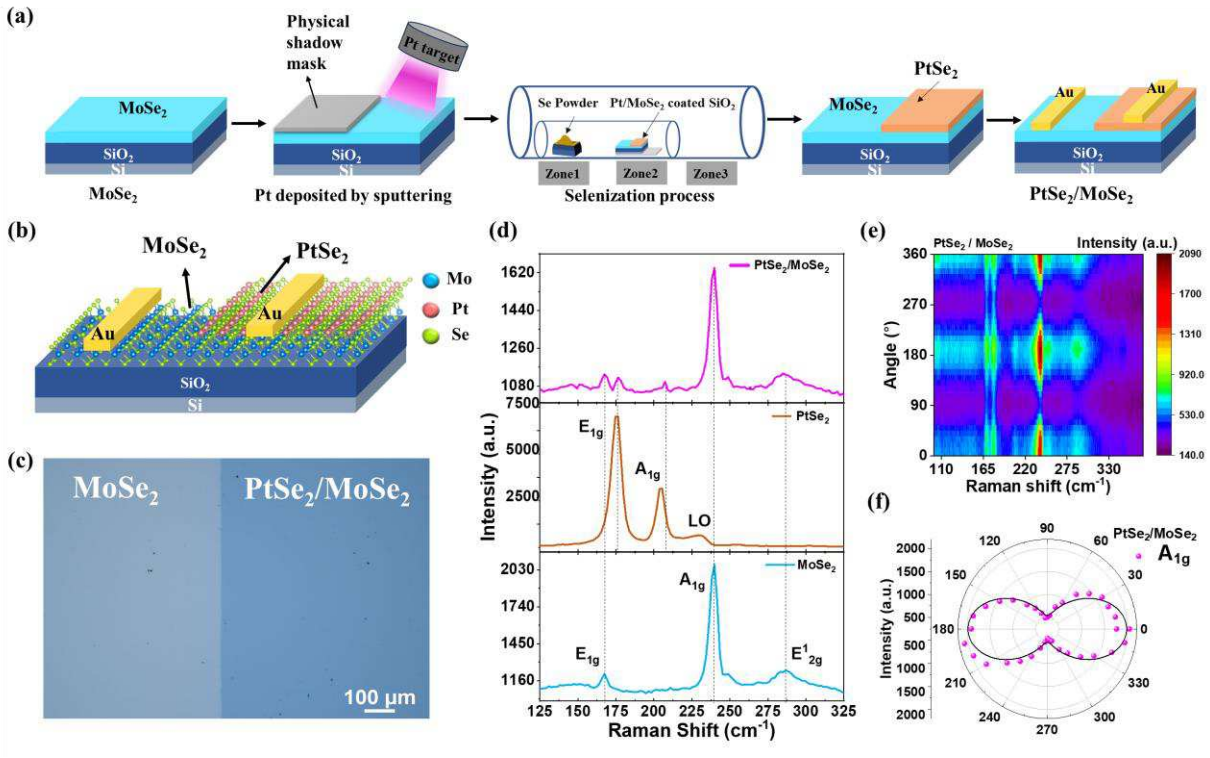


Figure 1. **(a)** Schematic diagram of experimental setup for the thermally assisted conversion (TAC) growth of $PtSe_2/MoSe_2$ thin films with Au (100 nm) electrodes. **(b)** Schematic diagram of $PtSe_2/MoSe_2$ heterostructure device. **(c)** Optical images highlighting the distinct contrast at

the interface of $MoSe_2$ and $PtSe_2$ films. **(d)** Raman spectra confirming the characteristic vibrational modes of $PtSe_2$, $MoSe_2$, and the $PtSe_2/MoSe_2$ heterostructure, indicating successful heterojunction formation. **(e)** Angle-resolved polarized Raman intensity map of $PtSe_2/MoSe_2$ heterostructure. **(f)** The polar plot of the Raman peak intensity (A_{1g} mode) at ~239 cm^{-1} as a function of polarization angle.

To determine the film thickness, atomic force microscopy (AFM) was used. The thicknesses were found to be approximately ~11 nm and ~16 nm for the pristine $MoSe_2$ film and $PtSe_2/MoSe_2$ heterostructure, respectively, as shown in Figure S3(a-d). Figure 2(a) depicts the comparison of the optical absorption spectra of bare $MoSe_2$, bare $PtSe_2$, and $PtSe_2/MoSe_2$ heterostructure[31, 45]. The heterostructure exhibits a higher absorption, suggesting that the interlayer coupling enhances its ability to capture incoming light. Tauc plots were constructed to estimate the band gap of $MoSe_2$, as shown in Figure S4(a). Subsequently, XPS analysis was performed to evaluate the chemical environment of the $MoSe_2$ and $PtSe_2$, as shown in Figure 2(b-f). The C 1s peak at 284.8 eV was used as a reference for charge calibration. In the Mo 3d spectrum, two prominent peaks are observed at 228.9 eV and 232 eV, corresponding to the Mo $3d_{5/2}$ and Mo $3d_{3/2}$ components, respectively, arising from spin-orbit coupling[51, 52]. In addition, two weaker peaks at 229.7 eV and 232.6 eV are attributed to Mo^{4+} in the MoO_2, as illustrated in Figure 2(b). The Se 3d spectra (see Figure 2(c)) exhibit peaks at 54.5 eV and 55.3 eV, characteristic of Se^{2-} in $MoSe_2$. Similarly, the O 1s spectrum reveals a peak at 531.0 eV, corresponding to the Mo-O bond in MoO_2, while an additional minor peak present may be due to surface-adsorbed hydroxyls (-OH) or ambient moisture exposure[52, 53, 54]. The $PtSe_2$ signatures are evident in Figure 2(e-f), where the Pt 4f spectrum shows a doublet centred at 72.6 eV ($4f_{7/2}$) and 75.9 eV ($4f_{5/2}$), and Se 3d peaks at 55.1 eV and 55.9 eV, exhibit a slight shift to higher binding energies compared to Mo-Se bonding, owing to the higher electronegativity of Pt [44, 45]. The valence band maximum (VBM) was determined from valence band spectra by

extrapolating the linear portion of the leading edge to the baseline and found to be approximately 0.8 eV (see Figure S4(b)). Furthermore, ultraviolet photoelectron spectroscopy (UPS) analysis (see Figure S4(c-d)) provided the work function of 4.84 eV for $MoSe_2$ and 5.29 eV for $PtSe_2$, respectively. The band diagram of $PtSe_2/MoSe_2$ before contact and after contact is illustrated in Figure S5(a-b). When $MoSe_2$ and $PtSe_2$ come into contact, charge transfer occurs until their Fermi levels equilibrate. Owing to the higher work function of $PtSe_2$, electrons flow from $MoSe_2$ to $PtSe_2$, resulting in a downward band bending toward the $MoSe_2$ side.

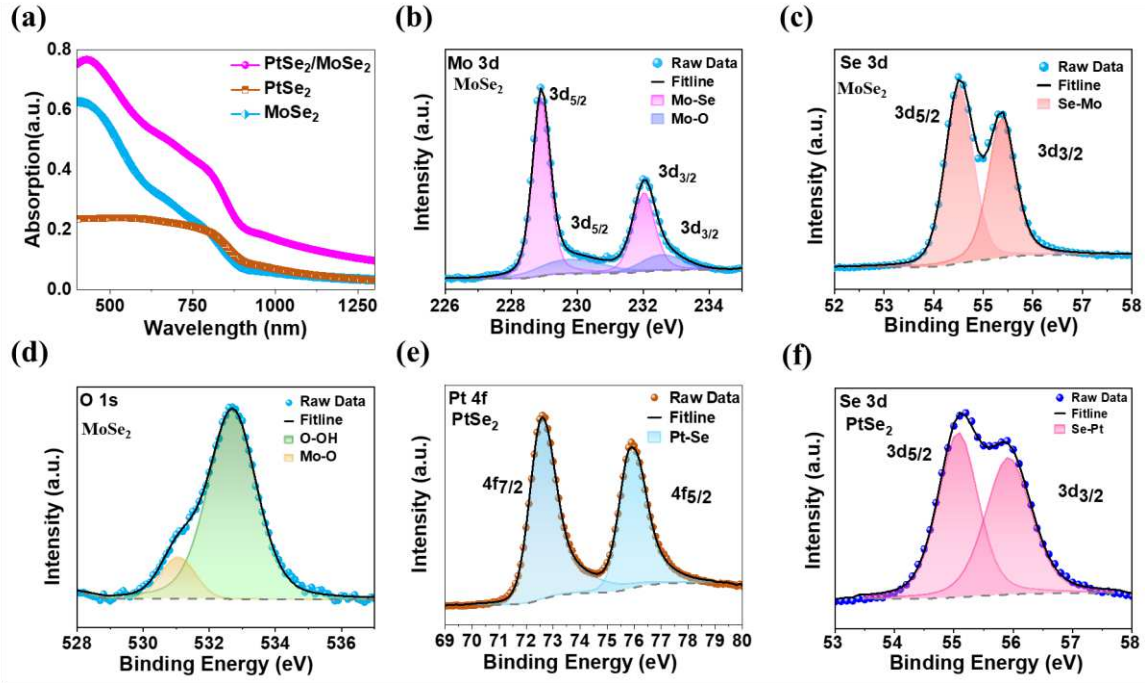


Figure 2. **(a)** Absorption comparison of bare $MoSe_2$, $PtSe_2$ and $PtSe_2/MoSe_2$ heterostructure. XPS analysis of $MoSe_2$, $PtSe_2$ thin film: Core-level spectra of **(a)** Mo, **(b)** Se, **(c)** O, **(d)** Pt, **(e)** Se bond with Pt, confirming the chemical state in the film.

Finally, we fabricated the $PtSe_2/MoSe_2$ heterostructure device to evaluate its optoelectronic performance. Figure 3(a) displays the current-voltage (I-V) characteristics of the $PtSe_2/MoSe_2$ heterostructure photodetector in both linear and logarithmic scales under dark conditions. The nonlinear and rectifying nature of the I-V curves confirms the formation of an effective

heterojunction[36]. The rectification ratio is determined to be 106 at ± 5V. Additionally, the logarithmic I-V curves under dark and illuminated conditions across a wide range of wavelengths (400-1200 nm), shown in Figure 3(b), demonstrate its broadband photodetection capability. The linear I-V plot of $PtSe_2/MoSe_2$ heterostructure is shown in Figure S6(a), with an enlarged view from 0V to 5V. The broadband photodetection can arise from the combination of semiconducting $MoSe_2$, which absorbs visible light, and semi-metallic $PtSe_2$, which extends the photoresponse into the near-infrared, along with efficient carrier separation at the heterojunction interface[55]. Also, the linear I-V characteristics of the $MoSe_2$ device under dark and 400-1200 nm light illumination are demonstrated in Figure S6(b). In comparison to the $MoSe_2$ device, the heterostructure exhibits a significantly enhanced photocurrent, which increases by approximately three orders of magnitude ($\sim 10^3$) at -5V, as illustrated in Figure 3(c). The optical power densities used for photocurrent measurements (400-1200 nm) are listed in Table S1 (Supplementary information).

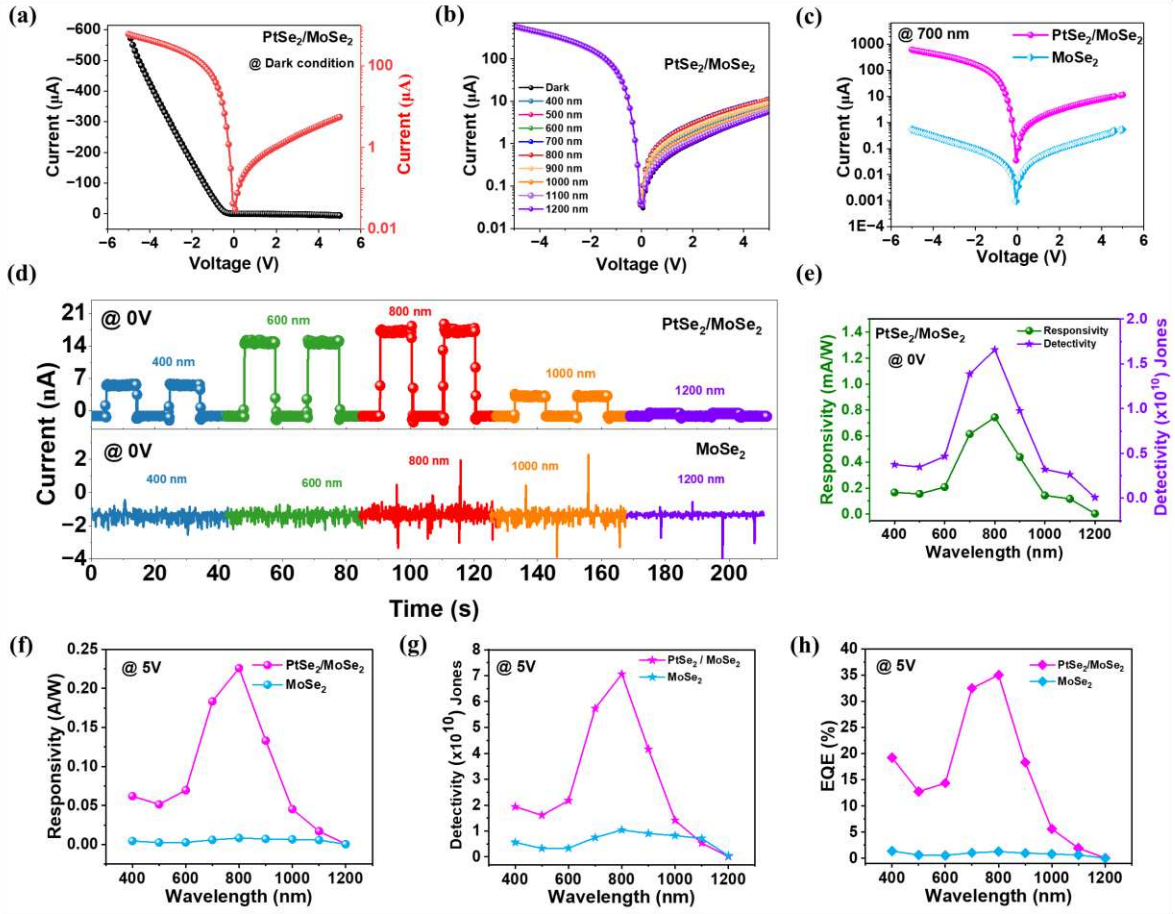


Figure 3. The Photoresponse of $PtSe_2/MoSe_2$ heterojunction: **(a)** Current-voltage (I-V) characteristics of the $PtSe_2/MoSe_2$ heterojunction were measured under dark conditions in logarithmic and linear plots. **(b)** I-V curves of the device under dark and illumination of varied wavelengths from 400 nm to 1200 nm. **(c)** Comparison of photocurrent for $MoSe_2$ and $PtSe_2/MoSe_2$ devices at 700 nm, highlighting the enhanced response of the heterostructure to the bare $MoSe_2$ device. **(d)** Comparison of the I-T characteristics of the devices under self-powered conditions from 400 nm to 1200 nm. **(e)** Responsivity and detectivity across wavelengths under self-powered conditions. **(f)** Enhanced responsivity of the heterojunction compared to the pristine $MoSe_2$ device at 5V bias. Comparison of the **(g)** detectivity and **(h)** EQE between the $PtSe_2/MoSe_2$ heterostructure and the pristine $MoSe_2$ device.

Figure 3(d) compares the time-dependent photoresponse of the $PtSe_2/MoSe_2$ heterostructure and bare $MoSe_2$ under self-bias conditions across a wavelength range of 400-1200 nm. The

heterostructure exhibits rapid and stable on/off switching without noticeable lag, enabled by the built-in field that facilitates true self-powered operation[31]. In contrast, the pristine $MoSe_2$ shows no measurable response under self-bias[40, 47]. Furthermore, the I-T characteristics of the heterostructure measured at 5V are shown in Figure S6(c). These results collectively demonstrate the device's broadband detection capability, fast response, and excellent operational stability, highlighting its strong potential for real-time photodetection applications.

To further elucidate the device performance of the $PtSe_2/MoSe_2$ photodetector, some figures of merit were calculated. Responsivity (R) is the ratio of photocurrent and the incident optical power, and is given as:

$$R = \frac{I_{light} - I_{dark}}{P.A} \quad \textbf{(2)}$$

Where, I_{dark} and I_{light} are the current in the dark and illumination, A is the effective area of the device, and P is the optical power intensity. Detectivity (D) indicates weak-signal detection capability:

$$D = \frac{\sqrt{A}R}{\sqrt{2eI_{dark}}} \quad \textbf{(3)}$$

Where 'e' is the elementary charge. External quantum efficiency (EQE) measures the conversion of incident photons into photogenerated charge carriers and is calculated as:

$$EQE = \frac{hcR}{e\lambda} \quad \textbf{(4)}$$

Where h is Planck's constant, c is the speed of light, and λ is the incident wavelength. Figure 3(e) shows that the $PtSe_2/MoSe_2$ heterojunction exhibits a high peak responsivity of 0.74 mA/W and a detectivity of 1.6×10^{10} Jones at 800 nm under self-biased conditions, confirming its suitability for weak-light photodetection. At a bias applied bias of 5V under 800 nm illumination, the responsivity increased to 0.23A/W, which is significantly (27 times) higher

than the bare $MoSe_2$ device, as shown in Figure 3(f). In addition, both the detectivity and EQE of the heterostructure show substantial improvement over the pristine $MoSe_2$ device, as depicted in Figure 3(g-h). These enhancements originate from the built-in electric field at the semimetal–semiconductor interface, which enables efficient carrier separation and collection, while the high mobility and broadband absorption of semi-metallic $PtSe_2$ further improve overall device performance.

To further investigate the photoexcited carrier dynamics, photoresponse measurements were performed on the $PtSe_2/MoSe_2$ heterostructure device by varying the incident light intensity. Figure 4(a-b) shows that the photocurrent increases monotonically with increasing incident optical power under 650 nm laser illumination at both 0V and 5V bias, confirming efficient photocarrier generation and collection. The corresponding temporal response under 532 nm laser illumination is presented in Figure S7(a-b), while the I-V characteristics of the heterostructure device under various light intensities are shown in Figure S7(c–d)). The relationship between photocurrent and power density is analyzed via a log-log plot, as illustrated in Figure 4(c), fitted using the power law[56]:

$$I_{ph} = A\phi^{\alpha} \quad \textbf{(5)}$$

where I_{ph} is the photocurrent, ϕ is the incident optical power density, A is a proportionality constant, and α is the dimensionless exponent that reveals the trap states density and recombination dynamics[57]. For an ideal trap-free photodetector, $\alpha = 1$, implying a linear relationship between photocurrent and optical power. Here, for the heterostructure device, the value of α increases from 0.53 at 0V to 0.62 at 5V, as demonstrated in Figure 4(c), indicating that an external bias enhances the built-in electric field, improves carrier collection, and partially suppresses trap-mediated recombination[57].

Another key figure of merit for photodetectors is response speed, quantified by the rise time (t_r) and fall time (t_f). These are defined as the time required for the photocurrent to increase from 10% to 90% of its peak value (rise time) upon light illumination or decrease from 90% to 10% upon light cessation (fall time). The temporal response of the heterostructure device was tested using a mechanical optical chopper synchronized with an oscilloscope, as shown in Figure 4(d). At 3kHz chopping frequency and 0V bias, the rise/fall times were found to be 97/54 μs (532 nm laser) and 68/66 μs (650 nm laser), as shown in Figure 4(e). while at a 5V bias, the response times decrease to 8/8 μs (532 nm laser) and 6 /6 μs (650 nm laser), indicating the ultra-fast detection capabilities of the $PtSe_2/MoSe_2$ heterostructure[31]. The devices may respond even faster, but the present testing equipment limits the lowest values to about 6 μs. The ultrafast photoresponse can be attributed to the high carrier mobility of the constituent films, efficient carrier separation driven by the built-in electric field, and minimal interface trap density at the van der Waals heterointerface. These factors collectively enable rapid carrier transport through the ultrathin heterostructure, leading to high-speed and efficient photodetection performance.[58, 59, 60].

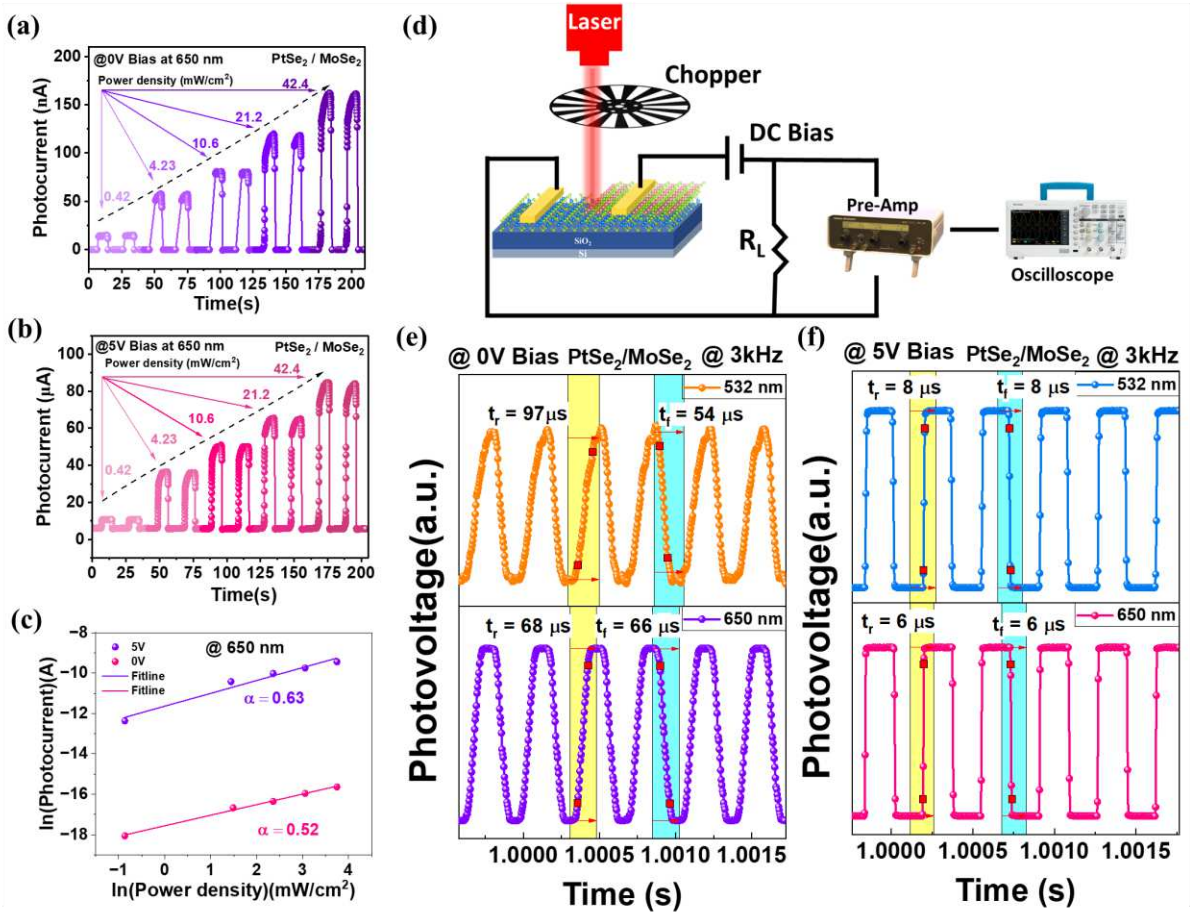


Figure 4: Power density-dependent temporal response of the $PtSe_2/MoSe_2$ heterostructure photodetector under illumination of 650 nm in **(a)** self-biased and **(b)** 5V bias conditions. **(c)** Power-law analysis of the measured photocurrent as a function of incident optical power at 0V and 5V applied bias for illumination at 650 nm. **(d)** Schematic representation of high-speed photodetection measurement setup. Temporal response of the device for 532 nm and 650 nm excitation measured using the mentioned set-up at **(e)** 0V bias and **(f)** 5V bias.

To elucidate the operating mechanism of the $PtSe_2/MoSe_2$ device under different bias conditions, the band alignment derived from XPS and UPS measurements is analysed. When $MoSe_2$ and $PtSe_2$ come into contact, charge transfer occurs until their Fermi levels align due to the high work function of $PtSe_2$, resulting in downward band bending toward the $MoSe_2$ side.

Hence, a Schottky barrier forms at the heterojunction and generates a built-in electric field from $MoSe_2$ to $PtSe_2$[31, 36]. So, under illumination, photogenerated electron-hole pairs are generated and efficiently separated by the built-in electric field, which drives electrons toward the $PtSe_2$ side and holes toward the $MoSe_2$ side, even in the absence of an external bias. Consequently, a measurable photocurrent is produced at zero bias (see Figure 5(a)) due to the internal potential difference. This demonstrates the self-powered behaviour of the $PtSe_2/MoSe_2$ heterojunction. Furthermore, when a forward bias is applied (see Figure 5 (b)), the barrier height decreases, electrons come out of the barrier from $MoSe_2$, and there is a thermionic emission or jumping of electrons over a barrier, which increases the value of current, as clearly seen in the I-V characteristics of the heterojunction, see Figure 3(a). In contrast, under reverse bias (see Figure 5(c)), the built-in field aligns with the external field, thereby enhancing band bending on the $MoSe_2$ side and the Fermi level shifts downward. Hence, this thicker barrier suppresses carrier transport, producing clear rectifying behaviour. The enhanced electric field in the barrier region promotes carrier drift, with photocurrent primarily arising from the drift of minority carriers[31, 36, 49].

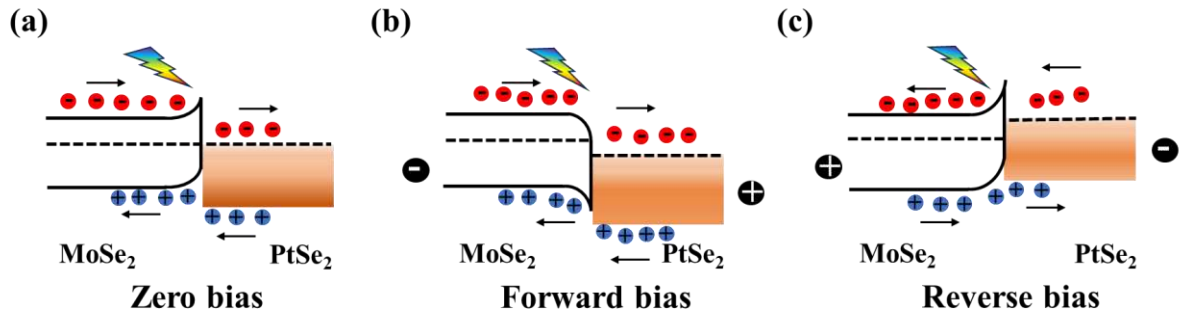


Figure 5: Charge transport mechanism in the $PtSe_2/MoSe_2$ heterojunction: schematics of band diagrams of $PtSe_2/MoSe_2$ heterojunction under **(a)** zero bias, **(b)** forward bias and **(c)** reverse bias conditions.

The strong interlayer coupling between $MoSe_2$ and $PtSe_2$ films enhanced the anisotropy in the $PtSe_2/MoSe_2$ heterostructure device enable device capable of polarization-sensitivity detection. Following angle-resolved polarized Raman spectroscopy analysis, the polarization-sensitive photoresponse characteristics of the $PtSe_2/MoSe_2$ heterostructure device were systematically investigated using the experimental configuration illustrated in Figure 6(a). The polarized photocurrent distribution of the $PtSe_2/MoSe_2$ heterojunction under 650 nm laser illumination at various applied bias voltages is shown in Figure 6(b) as a function of polarization angle. The photocurrent shows a 180˚ periodic dependence on the polarization angle for all bias conditions. The polarization ratio varies with applied voltages, indicating that both incident light polarization and the applied bias have a significant and combined impact on the device photoresponse[11, 49]. Figure 6(c-d) illustrates the polarized photocurrent as a function of polarization angle, confirming the polarization sensitive photoresponse of the heterostructure device. The photocurrent dependence on polarization angle conforms to the classic Malus law and is fitted via the sinusoidal function as [23, 27].

$$I(\theta) = I_{max}\cos^2(\theta + \varphi) + I_{min}sin^2(\theta + \varphi) \quad \textbf{(6)}$$

Where θ is the angle of polarization, φ is the fitting parameter, and I_{max} and I_{min} represent the maximum and minimum photocurrents. The heterostructure device shows a variation in the photocurrent by changing the polarization direction of the incident light. Under 532 nm laser illumination, the heterostructure device exhibits a maximum polarized photocurrent at a polarization angle of 140˚, whereas under 650 nm laser illumination, the maximum response shifts to 0˚. This shift in the polarization angle of maximum photocurrent indicates a clear wavelength-dependent anisotropy in the $PtSe_2/MoSe_2$ heterostructure. To further verify this wavelength-dependent behavior, the device was illuminated with monochromatic polarized light while systematically varying the wavelength from 400 nm to 800 nm. As the wavelength increases, the polarization angle corresponding to the maximum photocurrent (ψ) at an applied

bias of 0V gradually shifts from approximately 60˚ to 160˚, as illustrated in Figure 6(e). The polarization-resolved photoresponse measured under self-biased conditions at different wavelengths is presented in Figure S8(a–i), while the corresponding measurements at a 5V bias are shown in Figure S9(a–i). This continuous rotation of the polarization axis with wavelength suggests that the dominant optical absorption and carrier transport directions evolve across the spectral range, highlighting wavelength-dependent anisotropic interactions within the $PtSe_2/MoSe_2$ heterostructure[11, 27, 61].

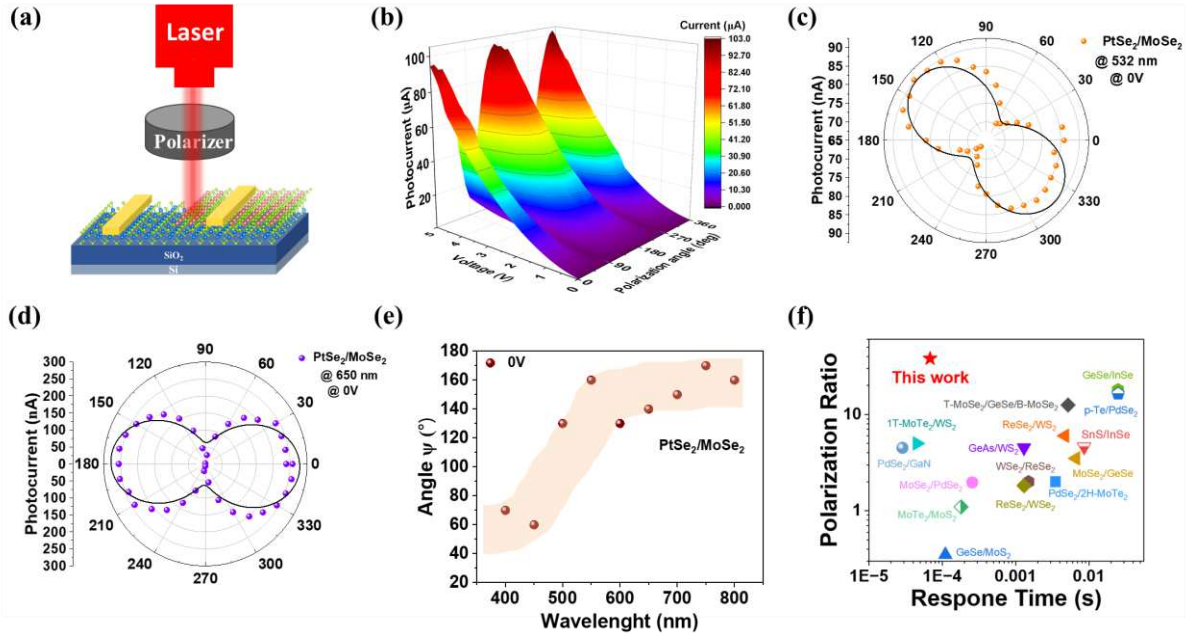


Figure 6: Polarisation-dependent study of $PtSe_2/MoSe_2$ heterostructure photodetector: **(a)** Schematic diagram of the experimental setup for polarization-resolved photocurrent measurement. **(b)** Photocurrent distribution as a function of polarization angle under 650 nm illumination at various voltages (from 0 to 5V). The polarized photocurrents in a polar plot under self-powered conditions with an illumination of **(c)** 532 nm and **(d)** 650 nm. **(e)** Wavelength-dependent anisotropy of the device from 400-800 nm. **(f)** Comparison of polarization ratio and response time across a state-of-the-art self-powered polarization-sensitive

photodetector, highlighting a superior performance (PR~38) $PtSe_2/MoSe_2$ heterostructure device[4, 7, 11, 21, 26, 36, 40, 41, 42, 43, 47, 62, 63, 64, 65, 66, 67].

Qualitatively, one may understand the rotation of maxima as a function of incident photon energy (wavelength) by invoking the quantum mechanical picture. It basically involves interaction between electron-photon and electron-electron/phonon. In a simplistic picture, whenever a photon of a given wavelength impinges on the system, the electronic system absorbs this photon, and an electron-hole pair is created that results in a finite electron-photon interaction (H_{op}). After that electron goes to the excited state available, and here it may be scattered to another state via interactions with another electron or by creating or absorbing a phonon, resulting in an electron-electron ($H_{el\text{-}el}$) and/or electron-phonon interaction ($H_{el\text{-}ph}$). And finally, the electron will come back to the initial state and combine with the hole and emit the photon (electron-photon interaction; H_{op}). Within the first-order perturbation theory, the scattering of electrons by electrons and/or phonons is responsible for generating the current, assuming no impurity and defects are present; and as a result, it should be proportional to the factor given as $\propto \langle g|H_{op}|m'\rangle\langle m'|H_{el-el}\,/\,H_{el-ph}|m\rangle\langle m|H_{op}|g\rangle$ [68]. Where $|g\rangle$ is the ground state, and $|m\,/\,m'\rangle$ are the intermediate states; H_{op} and $H_{el-el/ph}$ are the electron-photon and electron-electron/phonon interactions, respectively. First and third term uses the dipole selection rule for the optical transition, and represent the electron-electron/phonon matrix element. Considering the electron-photon interaction within the dipole approximation, the electron-photon matrix element, $\langle m|H_{op}|g\rangle$, may be given as $\langle m|H_{op}|g\rangle \propto \vec{\varepsilon}_i.\langle m|\vec{\nabla}|g\rangle = \vec{\varepsilon}_i.\vec{D}_{mg}$ [69]. Where $\vec{\varepsilon}_i$ is the polarization vector of the incident light and $\vec{D}_{mg}\,(=\langle m|\vec{\nabla}|g\rangle)$ is a dipole vector. From the above equation, it is clear that to have a finite contribution from the electron-photon matrix term, the dipole matrix element $\vec{D}_{mg}$

should have a finite component along the direction of light polarization $\vec{\varepsilon}_i$. This may also be used to understand which states, $|g\rangle, |m\rangle$, from the available energy bands be involved in this transition of electron for a given energy of the incident photon and direction $\vec{\varepsilon}_i$; and the different possible allowed values of the matrix element $\langle m|H_{op}|g\rangle$ for varying incident photon energy as well as polarization direction. This suggests that by changing incident photon energy as well as polarization the electron-photon matrix element may change and give rise to the change in the photocurrent polarization as seen here experimentally. Also, the electron-electron/phonon matrix element may also change with the change in the incident photon energy and polarization. For the case of TMDCs, the selection of the intermediate states is readily possible because of the existence of many energy bands with different symmetries within a short range of energy. Our results also open an opportunity to develop a full-fledged theoretical model by taking into consideration the electron-electron/phonon/impurity scattering matrix element for a quantitative understanding.

The polarization ratio (PR) is a key parameter, characterizing the anisotropy of the polarization response in the detection system[20] and is defined as:

$$\mathrm{PR} = \frac{\mathrm{I_{max}}}{\mathrm{I_{min}}} \quad \textbf{(5)}$$

Remarkably, the polarization ratio of the heterostructure device under self-biased conditions at 650 nm laser is extracted to be ~38, which appreciatively satisfies the demand of high-resolution photodetection. Moreover, the device exhibits a significant polarization ratio of ~1.3 at a 532 nm laser under 0V bias. Figure S10(a-b) illustrate that the device polarization ratio is around ~1.6 (for 532 nm laser) to ~9.2 (for 650 nm laser) at a 5V bias. A comparison of the polarization-sensivity of the self-powered $PtSe_2/MoSe_2$ photodetector is presented in Figure 6(f) and summarized in Table 2 of the supplementary information. The $PtSe_2/MoSe_2$

heterostructure exhibits a tremendously enhanced polarization sensitivity compared to other reported 2D materials and heterostructure-based photodetectors.

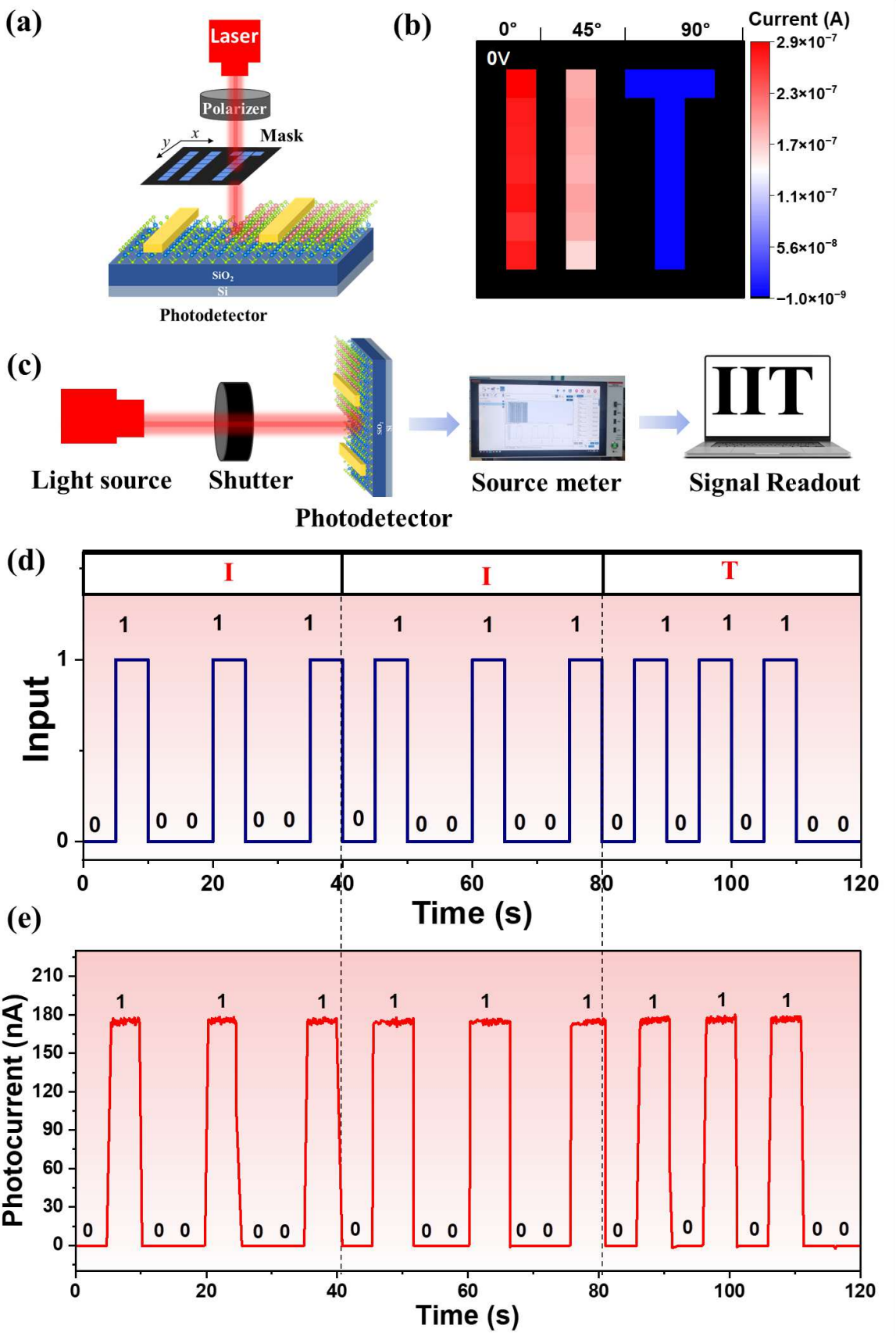

(a)
Laser
Polarizer
Mask
y
x
SiO2
Si
Photodetector
(b)
0°
45°
90°
0V
Current (A)
2.9×10−7
2.3×10−7
1.7×10−7
1.1×10−7
5.6×10−8
−1.0×10−9
(c)
Light source
Shutter
Photodetector
Source meter
IIT
Signal Readout
(d)
I
I
T
Input
Time (s)
(e)
Photocurrent (nA)
Time (s)

Figure 7: Imaging and optical communication applications of the $PtSe_2/MoSe_2$ device. **(a)** Schematic illustration of the experimental setup for polarization-resolved imaging measurements. **(b)** Polar contour image result of target letter "IIT" recorded under incident light polarization angles of 0˚, 45˚ and 90˚, respectively. **(c)** Schematic diagram of the intensity-modulated optical communication systems based on the $PtSe_2/MoSe_2$ device. **(d)** Time-dependent control signal of the shutter corresponding to the ASCII-coded transmission of the information "IIT." **(e)** Received electrical output signals of the intensity-encoded optical communication system ("1" = light on, "0" = light off), demonstrating accurate signal reconstruction.

The exceptional polarization performance of the heterostructure device was further explored through polarization-resolved imaging experiments, as illustrated in Figure 7(a). Under self-biased conditions, a laser beam was passed through a linear polarizer and then a mask patterned with the letters "IIT", which was translated in the *x–y* plane between the polarizer and the device, and the corresponding position-dependent photocurrent of the device was recorded at polarization angles of 0˚, 45˚, and 90˚. The resulting polarization-dependent photocurrent mapping imaging data are shown in Figure 7(b) and Figure S11(a–c) for 0V, and in Figure S11(d–f) for a bias of 5V. As the polarization angle is varied from 0˚ to 90˚, the reconstructed images display pronounced contrast variations, highlighting the robust polarization-sensitive optoelectronic imaging capability of the $PtSe_2/MoSe_2$ heterostructure, which is promising for high-fidelity imaging and multidimensional optoelectronic applications[23, 40].

Building upon its superior photoresponse characteristics, the device was further employed in optical communication applications. Optical communication utilizes intensity-modulated laser signals for data transmission, offering advantages such as wide bandwidth, energy efficiency, and immunity to electromagnetic interference. Owing to its broadband photoresponse (400-1200 nm), high sensitivity, and fast response speed, the $PtSe_2/MoSe_2$ vdWs heterojunction

photodetector was used as a receiver for American Standard Code for Information Interchange (ASCII)-encoded information transmission. A schematic illustration of the experimental setup is presented in Figure 7(c). As shown in Figure 7(d), a 650 nm laser beam was modulated by a time-controlled shutter to generate a binary sequence corresponding to the letters "IIT." The incident optical pulses were converted into electrical signals by the device and subsequently decoded through ASCII conversion. The reconstructed output signals (see Figure 7(e)) exhibit clear and undistorted pulse waveforms that closely match the input modulation sequence, confirming the high fidelity and fast response of the communication system. Overall, these findings demonstrate the multifunctional capability of the $PtSe_2/MoSe_2$ heterojunction photodetector in both polarization-sensitive imaging and high-accuracy optical communication applications.

Conclusion

In summary, we have successfully fabricated a $PtSe_2/MoSe_2$ van der Waals heterostructures device that simultaneously achieves broadband (400–1200 nm), self-powered, and highly polarization sensitive photodetection, addressing key challenges in polarization-sensitive photodetectors. The semimetal-semiconductor interface between $PtSe_2$ and $MoSe_2$ generates a strong built-in electric field and enables direction-selective charge transport. This intrinsic built-in field facilitates self-powered operation without the need for an external bias. Under self-powered mode, the device delivers a responsivity of 0.74 mA/W, a high detectivity of 1.6×10^{10} Jones, and ultra-fast response speeds with rise/decay time of 65/65 μs. Owing to the narrow band gap of $PtSe_2$ and broadband absorption of $MoSe_2$, the heterostructure demonstrates efficient photoresponse across the visible to near-infrared range. Strong optical anisotropy is further confirmed by angle-resolved polarization measurements, providing an effective route toward advanced polarized optoelectronic functionalities. Notably, the device achieves extremely high polarization ratios of ~38 in self-powered operation, as verified by angle-

resolved photoresponse measurements. The observed wavelength-dependent anisotropy (400 nm to 800 nm) and bias-tunable polarization sensitivity enable multifunctional device operation. Overall, the $PtSe_2/MoSe_2$ heterostructure platform establishes a benchmark for next-generation broadband, self-powered, polarization-resolved photodetection imaging and optical communications, for future compact optoelectronic systems.

Acknowledgment

The authors would like to express their sincere gratitude for the funding received from the Anusandhan National Research Foundation (ANRF) under the Advanced Research Grant (ARG) scheme with Project No. ANRF/ARG/2025/002092/PS. We also thank the Central Research Facility, IIT Ropar, for characterization facilities.

Conflict of Interest

The authors declare no conflict of interest.

Author Contributions

Priya Rani: Conceptualization, Methodology, Data curation, Visualization, Investigation, Writing—original draft. **Rohit Dahiya:** Conceptualization, Methodology, Data curation, Visualization, Investigation, Writing—original draft. **Chaitanya B. Auti:** Data curation, Investigation, Writing—review & editing. **Pradeep Kumar:** Conceptualization, Supervision, Resources, Visualization, Writing - review & editing. **Mukesh Kumar:** Conceptualization, Supervision, Resources, Project Administration, Visualization, Funding acquisition, Writing - review & editing. All authors discussed the results and commented on the manuscript.

Data Availability Statement

The data that support the findings of this study are available from the corresponding author upon reasonable request.

References

1. Liu Z*, et al.* Versatile on-chip polarization-sensitive detection system for optical communication and artificial vision. *Light: Science & Applications* **14**, 68 (2025).

2. Akinwande D*, et al.* Graphene and two-dimensional materials for silicon technology. *Nature* **573**, 507-518 (2019).

3. Khan S*, et al.* 2D Heterostructures for Highly Efficient Photodetectors: From Advanced Synthesis to Characterizations, Mechanisms, and Device Applications. *Advanced Photonics Research* **3**, 2100342 (2022).

4. Xiong J*, et al.* Multifunctional GeAs/WS2 Heterojunctions for Highly Polarization-Sensitive Photodetectors in the Short-Wave Infrared Range. *ACS Applied Materials & Interfaces* **14**, 22607-22614 (2022).

5. Roy K*, et al.* Graphene–MoS2 hybrid structures for multifunctional photoresponsive memory devices. *Nature Nanotechnology* **8**, 826-830 (2013).

6. Du X, Wu H, Peng Z, Tan C, Yang L, Wang Z. Room-temperature polarization-sensitive photodetectors: Materials, device physics, and applications. *Materials Science and Engineering: R: Reports* **161**, 100839 (2024).

7. Zhao Q*, et al.* High performance polarization-sensitive self-powered imaging photodetectors based on a p-Te/n-MoSe2 van der Waals heterojunction with strong interlayer transition. *Materials Horizons* **8**, 3113-3123 (2021).

8. Ahsan U*, et al.* Advances in visible and ultraviolet self-powered photodetectors: exploring 2D materials and Janus heterostructures. *Nanoscale* **18**, 537-574 (2026).

9. Dai M*, et al.* Long-wave infrared photothermoelectric detectors with ultrahigh polarization sensitivity. *Nat Commun* **14**, 3421 (2023).

10. Fang W*, et al.* Bioinspired single-shot polarization photodetector based on four-directional grating arrays capped perovskite single-crystal thin film. *Science Advances* **10**, eadr5375.

11. Liu M*, et al.* Uncooled near- to long-wave-infrared polarization-sensitive photodetectors based on MoSe2/PdSe2 van der Waals heterostructures. *Nature Communications* **16**, 2774 (2025).

12. Konstantatos G, Sargent EH. Nanostructured materials for photon detection. *Nature Nanotechnology* **5**, 391-400 (2010).

13. Tong L*, et al.* Stable mid-infrared polarization imaging based on quasi-2D tellurium at room temperature. *Nature Communications* **11**, 2308 (2020).

14. Rogalski A. Toward third generation HgCdTe infrared detectors. *Journal of Alloys and Compounds* **371**, 53–57 (2004).

15. Jia BWEN, Tan K, Loke W, Wicaksono S, Yoon S. Integration of an InSb photodetector on Si via heteroepitaxy for the mid-infrared wavelength region. *Optics Express* **26**, 7227-7234 (2018).

16. Mouloua D*, et al.* Scalable InAs/InGaAs DWELL structures for broadband infrared emission spanning the E- to O-band. *Scientific Reports* **15**, 37470 (2025).

17. Wu D*, et al.* Phase-controlled van der Waals growth of wafer-scale 2D MoTe2 layers for integrated high-sensitivity broadband infrared photodetection. *Light: Science & Applications* **12**, 5 (2023).

18. Sizov F. Terahertz radiation detectors: the state-of-the-art. *Semiconductor Science and Technology* **33**, 123001 (2018).

19. Long M, Wang P, Fang H, Hu W. Progress, Challenges, and Opportunities for 2D Material Based Photodetectors. *Advanced Functional Materials* **29**, 1803807 (2019).

20. Yu L, Dong H, Zhang W, Zheng Z, Liang Y, Yao J. Development and challenges of polarization-sensitive photodetectors based on 2D materials. *Nanoscale Horizons* **10**, 847-872 (2025).

21. Wu J*, et al.* Engineering the Polarization Sensitivity in All-2D Photodetectors Composed of Semimetal MoTe2 and Semiconductor WS2. *Advanced Optical Materials* **10**, 2201902 (2022).

22. Wang P*, et al.* Sensing Infrared Photons at Room Temperature: From Bulk Materials to Atomic Layers. *Small* **15**, 1904396 (2019).

23. Kang J*, et al.* In Situ Selenization-Engineered PtSe2/PdSe2 Heterostructures for Short-Wave Infrared Polarization-Sensitive Photodetection and Information Transmission. *Advanced Optical Materials* **n/a**, e02967 (2025).

24. Chhowalla M, Shin HS, Eda G, Li L-J, Loh KP, Zhang H. The chemistry of two-dimensional layered transition metal dichalcogenide nanosheets. *Nature Chemistry* **5**, 263-275 (2013).

25. Xu J, Zhang Z, Zhang W, Chen Z. Recent Progress of Self-Powered Optoelectronic Devices Based on 2D Materials (2024).

26. Ahn J*, et al.* Near-Infrared Self-Powered Linearly Polarized Photodetection and Digital Incoherent Holography Using WSe2/ReSe2 van der Waals Heterostructure. *ACS Nano* **15**, 17917-17925 (2021).

27. Li Z, Xu B, Liang D, Pan A. Polarization-Dependent Optical Properties and Optoelectronic Devices of 2D Materials. *Research (Wash D C)* **2020**, 5464258 (2020).

28. Yu I*, et al. Polarization-selective photodetector based on topological insulators for secure optical communications and sensing applications* (2024).

29. Liu J, Xia F, Xiao D, García de Abajo FJ, Sun D. Semimetals for high-performance photodetection. *Nature Materials* **19**, 830-837 (2020).

30. Wang J*, et al.* Enhanced exciton diffusion from interlayer charge-transfer transitions in PtSe2/MoSe2 van der Waals heterojunction. *Nano Research* **16**, 12809-12816 (2023).

31. Che M*, et al.* High-Efficiency Self-Powered Broadband Photodetector Based on PtSe2/MoSe2 Heterojunction. *ACS Photonics* **11**, 1693-1702 (2024).

32. Dong Q, Zhang Y, Wang F, Wang QJ. High-Performance Polarization-Sensitive Mid-Infrared Photodetection Based on a BP/PtSe2 van der Waals Heterostructure. *Advanced Optical Materials* **13**, e01489 (2025).

33. Liang L*, et al.* Heterointerface Engineering in Electromagnetic Absorbers: New Insights and Opportunities. *Advanced Materials* **34**, 2106195 (2022).

34. Ahn J, Yeon E, Hwang DK. Recent Progress in 2D Heterostructures for High-Performance Photodetectors and Their Applications. *Advanced Optical Materials* **13**, 2403412 (2025).

35. Kang J*, et al.* In Situ Selenization-Engineered PtSe2/PdSe2 Heterostructures for Short-Wave Infrared Polarization-Sensitive Photodetection and Information Transmission. *Advanced Optical Materials* **14**, e02967 (2026).

36. Gao P*, et al.* MoTe2/MoSe2 vdW Schottky Photodetector for Polarized Photodetection. *Chip*, 100147 (2025).

37. Awasthi C, Khan A, Islam SS. PdSe2/MoSe2: a promising van der Waals heterostructure for field effect transistor application. *Nanotechnology* **35**, 195202 (2024).

38. Ornelas CD*, et al.* Ultrafast Photocurrent Response and High Detectivity in Two-Dimensional MoSe2-based Heterojunctions. *ACS Applied Materials & Interfaces* **12**, 46476-46482 (2020).

39. Wu Y*, et al.* Van der Waals integration inch-scale 2D MoSe2 layers on Si for highly-sensitive broadband photodetection and imaging. *Nano Research* **16**, 11422-11429 (2023).

40. An K*, et al.* High-Performance Self-Driven Polarization-Sensitive Imaging Photodetectors based on Fully Depleted T-MoSe2/GeSe/B-MoSe2 Van der Waals Dual-Heterojunction. *Advanced Functional Materials* **34**, 2409331 (2024).

41. Wang P*, et al.* Anisotropic Te/PdSe2 Van Der Waals Heterojunction for Self-Powered Broadband and Polarization-Sensitive Photodetection. *Small* **20**, 2401216 (2024).

42. Wu D*, et al.* In Situ Fabrication of PdSe2/GaN Schottky Junction for Polarization-Sensitive Ultraviolet Photodetection with High Dichroic Ratio. *ACS Nano* **16**, 5545-5555 (2022).

43. Xin Y*, et al.* Polarization-Sensitive Self-Powered Type-II GeSe/MoS2 van der Waals Heterojunction Photodetector. *ACS Applied Materials & Interfaces* **12**, 15406-15413 (2020).

44. Dionisiev I, Marinova V, Buchkov K, Dikov H, Avramova I, Dimitrov D. Synthesis and Characterizations of 2D Platinum Diselenide. *Materials Proceedings* **2**, 22 (2020).

45. Bassi G, Dahiya R, Chakkar A, Kumar P, Kumar M. *Large Area, Ultrafast, Suppressed Dark Current and High-Performance Ptse2/Mos2 Van Der Waals Heterostructure Based Visible to Nir Broadband Photodetector* (2024).

46. Ciarrocchi A, Avsar A, Ovchinnikov D, Kis A. Thickness-modulated metal-to-semiconductor transformation in a transition metal dichalcogenide. *Nature Communications* **9**, 919 (2018).

47. Kong L*, et al.* Polarization-Sensitive, Self-Powered, and Broadband Semimetal MoTe2/MoS2 van der Waals Heterojunction for Photodetection and Imaging. *ACS Applied Materials & Interfaces* **15**, 43135-43144 (2023).

48. Yu J*, et al.* Direct Observation of the Linear Dichroism Transition in Two-Dimensional Palladium Diselenide. *Nano Letters* **20**, 1172-1182 (2020).

49. Zhang W*, et al.* Unraveling the Interfacial Carrier Behavior in PtSe2–MoSe2 Heterostructures: Insights from Combined Pump-Probe Spectroscopy and Scanning Tunneling Microscopy. *Advanced Science* **12**, 2500598 (2025).

50. Garrity O, Brumme T, Bergmann A, Korn T, Kusch P, Reich S. Interlayer Exciton–Phonon Coupling in MoSe2/WSe2 Heterostructures. *Nano Letters* **24**, 11853-11858 (2024).

51. Wadhwa R, Agrawal AV, Kushavah D, Mushtaq A, Pal SK, Kumar M. Investigation of charge transport and band alignment of MoS2-ReS2 heterointerface for high performance and self-driven broadband photodetection. *Applied Surface Science* **569**, 150949 (2021).

52. Hao Q, Cui G, Zhao Y, Bakenov Z. Flower-Like MoSe2/MoO2 Composite with High Capacity and Long-Term Stability for Lithium-Ion Battery (2019).

53. Wang X*, et al.* Chemical Vapor Deposition Growth of Crystalline Monolayer MoSe2. *ACS Nano* **8**, 5125-5131 (2014).

54. Wu Z, Tai G, Wang X, Hu T, Wang R, Guo W. Large-area synthesis and photoelectric properties of few-layer MoSe2 on molybdenum foils. *Nanotechnology* **29**, 125605 (2018).

55. Gong Y*, et al.* Two-Dimensional Platinum Diselenide: Synthesis, Emerging Applications, and Future Challenges. *Nano-Micro Letters* **12**, 174 (2020).

56. Kaur D, Dahiya R, Sheokand V, Bassi G, Kumar M. Ultrafast, self-powered and highly-stable PtS-Ga_2O_3 heterojunction photodetector for broad-spectrum sensing. *Surfaces and Interfaces* **61**, 106125 (2025).

57. Dahiya R*, et al.* Reverse-bias driven anomalous polarity switching in FeSi2/Ga2O3-NRs heterojunction based solar-blind photodetector. *Applied Surface Science* **720**, 165340 (2026).

58. Zhao Y*, et al.* High-Electron-Mobility and Air-Stable 2D Layered PtSe2 FETs. *Advanced Materials* **29**, 1604230 (2017).

59. Dutta T*, et al.* Electronic properties of 2D materials and their junctions. *Nano Materials Science* **6**, 1-23 (2024).

60. Banu S L, Veerapandy V, Fjellvåg H, Vajeeston P. First-Principles Insights into the Relative Stability, Physical Properties, and Chemical Properties of MoSe2. *ACS Omega* **8**, 13799-13812 (2023).

61. Kotha M, Kaloyeros A, Murray T, Gallis S. Wavelength-Dependent Anisotropic Optical Properties in Layered GaTe for Polarization-Sensitive Applications. *Advanced Photonics Research* **2**, 2100140 (2021).

62. Che M*, et al.* PdSe2/2H–MoTe2 Heterojunction Self-Powered Photodetector: Broadband Photodetection and Linear/Circular Polarization Capability. *ACS Nano* **18**, 30884-30895 (2024).

63. Jia C*, et al.* A self-powered high-performance photodetector based on a MoS2/GaAs heterojunction with high polarization sensitivity. *Journal of Materials Chemistry C* **7**, 3817-3821 (2019).

64. Xiong J*, et al.* High Performance Self-Driven Polarization-Sensitive Photodetectors Based on GeAs/InSe Heterojunction. *Advanced Optical Materials* **9**, 2101017 (2021).

65. Zeng L-H*, et al.* Multilayered PdSe2/Perovskite Schottky Junction for Fast, Self-Powered, Polarization-Sensitive, Broadband Photodetectors, and Image Sensor Application. *Advanced Science* **6**, 1901134 (2019).

66. Gao P*, et al.* Low-pressure PVD growth SnS/InSe vertical heterojunctions with type-II band alignment for typical nanoelectronics. *Nanoscale* **14**, 14603-14612 (2022).

67. Tang Y*, et al.* Distinctive Interfacial Charge Behavior and Versatile Photoresponse Performance in Isotropic/Anisotropic WS 2 /ReS 2 Heterojunctions. *ACS Applied Materials & Interfaces* **12**, 53475-53483 (2020).

68. Kumar D, Singh B, Kumar R, Kumar M, Kumar P. Anisotropic electron–photon–phonon coupling in layered MoS2. *Journal of Physics: Condensed Matter* **32**, 415702 (2020).

69. Sakurai JJ, Napolitano J. *Modern Quantum Mechanics*, 3 edn. Cambridge University Press (2020).

Supplementary Files

This is a list of supplementary files associated with this preprint. Click to download.

- Supporting.docx